Using patterned substrates to promote mixing in microchannels

Olga Kuksenok,[1] J. M. Yeomans,[2] and Anna C. Balazs[1]
[1]*Department of Chemical and Petroleum Engineering, University of Pittsburgh, Pittsburgh Pennsylvania 15261*
[2]*Theoretical Physics, University of Oxford, Keble Road, Oxford, OX1 3 NP, United Kingdom*
(Received 28 September 2001; published 12 February 2002)

Using a lattice Boltzmann model for fluid dynamics, we investigate the flow and phase behavior of a binary fluid moving over a patterned substrate within a microchannel. The binary fluid consists of two immiscible components, *A* and *B*, and this liquid is subjected to a Poiseuille flow. The substrate is decorated with a checkerboard pattern of *A*- and *B*-like patches. Through a coupling of hydrodynamics and thermodynamics, each component is driven to flow from the nonwettable domains to wettable regions. As a consequence, the *A* and *B* fluids undergo extensive mixing within the microchannels. We investigate how the degree of mixing depends on the size of the patches, the velocity of the imposed flow field, and the characteristics of the fluid. The results provide guidelines for creating localized ''mixing stations'' within microfluidic devices. The findings also reveal how a combination of imposed flow fields and surface patterning can be exploited to control the phase behavior of complex fluids.

DOI: 10.1103/PhysRevE.65.031502 PACS number(s): 64.75.+g, 47.11.+j

I. INTRODUCTION

Microfluidics involves the transport of minute quantities of liquids in networked channels that are 10–100 μm wide. Microfluidic systems lie at the heart of the lab-on-a-chip concept, which has the potential to shrink a room full of analytical instruments onto a compact, hand-held device. In order to facilitate the fabrication of microfluidic devices, it is important to develop predictive models that reveal the thermodynamic behavior and flow patterns of complex fluids in micron-sized channels. Of particular importance is using these models to design effective methods for mixing multicomponent fluids in the narrow chambers [1]. Extensive mixing between components in microchannels is difficult because the small dimensions of the system constrain the fluid to move in a laminar fashion (i.e., low Reynolds number flow). In the absence of turbulent flow, there is little mixing between the various confined fluids and thus, reagents and sample can only undergo limited interactions.

Numerous studies on thin films of binary fluids have shown that the phase behavior and morphology of the mixtures are significantly affected by the wetting properties of the underlying substrate (see, for example, Refs. [2–5]). Furthermore, a patterned surface with preferential wetting interactions can give rise to a rich variety of phenomena. For example, for thin films of binary fluids, the system can be driven to mimic the design in the underlying substrate [6,7]. In the studies cited above, the films are stationary, i.e., there is no imposed flow in the system. One expects that an external flow field would substantially modify the properties of patterned films. In terms of microfluidic applications, it may be possible to couple the effects of the substrate and the imposed flow to control the behavior of the mixture. In this paper, we use a computational model to analyze how the phase behavior of binary fluids under imposed flow is affected by chemically distinct patterns in the underlying surface. Through these studies, we show that patterned substrates can be exploited to drive extensive mixing of binary fluids flowing in microchannels.

One of the challenges inherent in modeling such a complex system is incorporating not only the interactions between the components but also, the interactions between the fluid and the substrate, i.e., wettability and surface tension, which play a dominant role in the behavior of confined fluids [8–15]. In addition, the model must describe the complicated micron-scale dynamics that arise from the above interactions. To capture these different features, we adopt the lattice Boltzmann approach, a simulation technique for fluid dynamics. This model captures the thermodynamic behavior of multiphase fluids [16] and can predict flow patterns in micron-sized pores [17]. Below, we introduce a method for including the wetting interactions between the fluids and the underlying substrate. Thus, we can develop correlations among surface wettability, phase behavior and flow patterns in the system.

II. THE MODEL

We consider two immiscible fluids [18], *A* and *B*, moving through the microchannel shown in Fig. 1, which represents a top-down view of the system. A Poiseuille flow is imposed on the fluids by applying a constant pressure gradient along the *x* direction. The ''floor'' of the channel is patterned with chemically distinct patches. In particular, a *B* patch (which

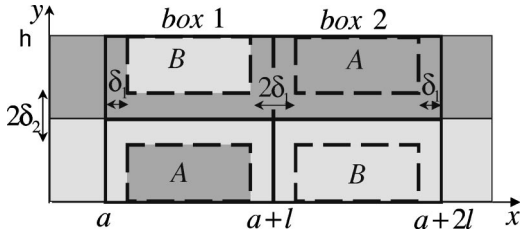

FIG. 1. Schematic drawing of the channel filled with an *A*/*B* binary fluid. Black represents the *A*-rich phase and white indicates the *B*-rich phase. Boxes 1 and 2 mark the pairs of chemically distinct patches. Letters within each box indicate the chemical nature (*A*- or *B*-like) of the patch.

preferentially attracts the *B* component) is introduced within the *A* stream and an *A* patch (which preferentially attracts the *A* component) is placed within the *B* stream. The contiguous *A* and *B* patches constitute the region marked ''box 1,'' which spans the width of the channel (see Fig. 1). In the adjacent ''box 2,'' the arrangement of the patches is reversed, so that entire pattern resembles a 2×2 checkerboard. Experimentally such chemically distinct regions can be created through microcontact printing [19] or a combination of photolithography and self-assembled monolayer chemistry [20].

The dynamics of the binary fluid inside the channel in Fig. 1 are described by a Navier-Stokes equation [Eq. (1)] and a convection-diffusion equation [Eq. (2)] for the order parameter, which characterizes the local composition of the binary fluid, $\phi=\rho^0(\mathbf{r})-\rho^1(\mathbf{r})$, where $\rho^0(\mathbf{r})$ and $\rho^1(\mathbf{r})$ are the number densities of each component. Here, we assume that the fluid is incompressible and the system is isothermal; under these conditions, Eqs. (1) and (2) can be written as [21]

$$\rho\partial_t(\vec{u})+\rho(\vec{u}\nabla)\vec{u}=-\nabla\mathbf{P}+\eta\Delta\vec{u}+\vec{H}, \tag{1}$$

$$\partial_t(\phi)+\nabla(\phi\vec{u})=D\Delta\mu_\phi, \tag{2}$$

where $\rho=\rho^0+\rho^1$ is the total fluid density, $\vec{u}$ is the fluid velocity, η is the viscosity, and D is the diffusivity. The chemical potential μ_ϕ, pressure $\mathbf{P}$, and the external force $\vec{H}$ that act on the element of fluid are determined from the expression for the free energy of the system. We define the free energy F as

$$F=\int d\mathbf{r}[\psi(\phi,\rho,T)+k/2(\nabla\phi)^2+V(\phi,\mathbf{r})]. \tag{3}$$

The term $\psi(\phi,\rho,T)$ describes the free energy of the homogeneous system and includes the repulsive term between the two components, $\lambda\rho^0\rho^1$, where λ is the strength of the repulsion,

$$\psi(\phi,\rho,T)=\frac{\lambda\rho}{4}\left(1-\frac{\phi^2}{\rho^2}\right)-T\rho+\frac{T}{2}(\rho+\phi)\ln\left(\frac{\rho+\phi}{2}\right)+\frac{T}{2}(\rho-\phi)\ln\left(\frac{\rho-\phi}{2}\right). \tag{4}$$

The second term in Eq. (3) describes the energy of the interface between the two phases; the coefficient k is a measure of the surface tension. The last term in Eq. (3) is an interaction potential that introduces the coupling between the order parameter and the chemically distinct patches. It is through this term that we model the preferential wetting interactions.

The wetting interactions take the following form (see Fig. 1): in box 1, the *B*-rich phase is preferentially favorable for $y<h/2$ and the *A*-rich phase is favored for $y>h/2$; in box 2, the situation is reversed. For the coupling potential inside each patch (marked as dashed boxes on Fig. 1), we choose the following simple forms [23]. In the *A* patches,

$$V(\phi,x,y)=C(\phi-\phi_A)^2, \tag{5}$$

where the constant C gives the strength of the interaction and ϕ_A is the value of the equilibrium order parameter for the *A* phase. In the *B* patches,

$$V(\phi,x,y)=C(\phi-\phi_B)^2, \tag{6}$$

where ϕ_B is the value of the equilibrium order parameter for the *B* phase. At the edges of the patches, these coupling potentials decay exponentially,which leads to an overlap of both potentials in the intermediate regions of width $2\delta_1$ and $2\delta_2$ (see Fig. 1). In these regions, the potentials have the following forms:

$$V(\phi,x,y)=\begin{cases} V(\phi,a+\delta_1,y)e^{-|x-(a+\delta_1)|/r} & \text{if } x<a+\delta_1,\\ V(\phi,a+2l-\delta_1,y)e^{-|x-(a+2l-\delta_1)|/r} & \text{if } x>a+2l-\delta_1,\\ V(\phi,x_-,y)e^{-|x-x_-|/r}+V(\phi,x_+,y)e^{-|x-x_+|/r} & \text{if } x_-<x<x_+,\\ V(\phi,x,y_-)e^{-|y-y_-|/r}+V(\phi,x,y_+)e^{-|y-y_+|/r} & \text{if } y_-<y<y_+, \end{cases}$$

where $x_\pm=a+l\pm\delta_1$, $y_\pm=h/2\pm\delta_2$.

We have examined different types of potentials and found that the particular choice for the form of potential does not play a crucial role in the dynamics described below. In particular, similar results can be obtained with a potential centered in the middle of each patch and exhibiting an exponential decay from this center [24]. The most important feature in the choice of the potential is the ''checkerboard'' design and the assumption of some overlap between the patches. This overlap causes a smooth change of the order parameter between the patches in the thermodynamic limit.

Outside the patterned domain, the fluid components undergo phase separation at temperatures smaller than the critical value $T<\lambda/2$. At the two-phase coexistence, the equilibrium values of the order parameter is $\phi_A=\phi_0$ for the *A*-rich phase and $\phi_B=-\phi_0$ for the *B*-rich phase.

The chemical potential and pressure tensor are derived from the free energy as

$$\mu^{\phi}=\delta F/\delta\phi=\frac{\partial\psi(\rho,\phi)}{\partial\phi}+\frac{\partial V(\phi,\mathbf{r})}{\partial\phi}-k\partial_\alpha\partial_\alpha\phi, \quad (7)$$

$$P_{\alpha\beta}=p_0\delta_{\alpha\beta}+k(\partial_\alpha\phi\partial_\beta\phi-1/2\partial_\gamma\phi\partial_\gamma\phi\delta_{\alpha\beta}-\phi\partial_\gamma\partial_\gamma\phi\delta_{\alpha\beta}), \quad (8)$$

and

$$p_0=\left[-\psi(\phi,\rho,T)-V(\phi,\mathbf{r})+\rho\frac{\partial\psi(\phi,\rho,T)}{\partial\rho}+\phi\frac{\partial\psi(\phi,\rho,T)}{\partial\phi}+\phi\frac{\partial V(\phi,\mathbf{r})}{\partial\phi}\right]. \quad (9)$$

Finally, we define the force term in Eq. (1) as $H_x=-\partial_x V+f_p$ and $H_y=-\partial_y V$. Here $-f_p$ is the constant pressure gradient needed to impose Poiseuille flow along the x axis. (It should be noted that the extra force and pressure tensor can be derived from the two-fluid model for the dynamics of a binary mixture [25].)

At the channel's boundaries ($y=0$ and $y=h$), we impose $\vec{u}=0$ and $\partial_y\phi=0$. In the x direction, we impose periodic boundary conditions ($x=0$ is the same point as $x=L_x$).

To find the numerical solution for Eq. (1) and (2), we adopt the lattice Boltzmann algorithm. In this method, the physical variables (density, order parameter, and velocity) are described through sets of distribution functions that are discrete in space and time. The evolution of each distribution function obeys the Boltzmann-like equation. Below, we describe this method in more detail.

III. LATTICE BOLTZMANN ALGORITHM

To model the binary fluid, we define two distribution functions $f_i(\vec{x})$ and $g_i(\vec{x})$ on each lattice site $\vec{x}$. We use the nine-velocity model with velocity vectors $\vec{e}_i=(\pm1,0)$, $(0,\pm1)$,$(\pm1,\pm1)$,$(0,0)$. Physical variables are defined as

$$\rho=\sum_i f_i, \quad \rho u_\alpha=\sum_i f_i e_{i\alpha}, \quad \phi=\sum_i g_i. \quad (10)$$

We use the improved (predictor-corrector) scheme [26] to describe the evolution of the distribution functions during a time step Δt. The evolution equations are

$$f_i(\vec{x}+\vec{e}_i\Delta t,t+\Delta t)-f_i(\vec{x},t)=\frac{\Delta t}{2}[\mathcal{C}_{fi}(\vec{x},t,\{f_i\})+\mathcal{C}_{fi}(\vec{x}+\vec{e}_i\Delta t,t+\Delta t,\{f_i^*\})] \quad (11)$$

and

$$g_i(\vec{x}+\vec{e}_i\Delta t,t+\Delta t)-g_i(\vec{x},t)=\frac{\Delta t}{2}[\mathcal{C}_{gi}(\vec{x},t,\{f_i\})+\mathcal{C}_{gi}(\vec{x}+\vec{e}_i\Delta t,t+\Delta t,\{g_i^*\})], \quad (12)$$

where f_i^* and g_i^* are first order approximations to $f_i(\vec{x}+\vec{e}_i\Delta t,t+\Delta t)$ and $g_i(\vec{x}+\vec{e}_i\Delta t,t+\Delta t)$, respectively. The collision operators are

$$\mathcal{C}_{fi}(\vec{x},t,\{f_i\})=-\frac{1}{\tau_f}[f_i(\vec{x},t)-f_i^{eq}(\vec{x},t,\{f_i\}))+h_i(\vec{x},t,\{f_i\})], \quad (13)$$

$$\mathcal{C}_{gi}(\vec{x},t,\{g_i\})=-\frac{1}{\tau_g}[g_i(\vec{x},t)-g_i^{eq}(\vec{x},t,\{g_i\})]. \quad (14)$$

The predictor-corrector scheme has advantages over the standard discretization of the evolution equations. First, the scheme is more stable and second, it allows us to write the constraints for the equilibrium force term in the collision operator in a rather straightforward, simple form (see below).

The conservation of number density for each component and the conservation of momentum for the bulk are imposed through the following equations:

$$\sum_i f_i^{eq}=\rho, \quad \sum_i f_i^{eq}e_{i\alpha}=\rho u_\alpha, \quad \sum_i g_i^{eq}=\phi. \quad (15)$$

In addition, in the lattice Boltzmann model, we impose the following constraints [22–26]:

$$\sum_i f_i^{eq}e_{i\alpha}e_{i\beta}=P_{\alpha\beta}+\rho u_\alpha u_\beta, \quad (16)$$

$$\sum_i h_i=0, \ \sum_i h_i e_{i\alpha}=H_\alpha, \ \sum_i h_i e_{i\alpha}e_{i\beta}=0, \quad (17)$$

$$\sum_i g_i^{eq}e_{i\alpha}=\phi u_\alpha, \ \sum_i g_i^{eq}e_{i\alpha}e_{i\beta}=\Gamma\mu_\phi\delta_{\alpha\beta}+\phi u_\alpha u_\beta. \quad (18)$$

With the above constraints, expansion of Eqs. (11)–(12), up to second order in Δt, leads to both the Navier-Stokes equation [26] (where viscosity is defined as $\rho\tau_f/3$) and the following convection-diffusion equation (where the diffusion coefficient is $D=\Gamma\tau_g$):

$$\partial_t(\phi)+\boldsymbol{\nabla}_\alpha\phi u_\alpha=\tau_g\Gamma\Delta\mu_\phi-\tau_g\partial_\beta\left[\frac{\phi}{\rho}(\partial_\alpha P_{\alpha\beta}-H_\beta)\right]. \quad (19)$$

The additional term (last term on the right hand side of the above equation) is common to these lattice Boltzmann schemes ([22]), but it is small compared to the other terms.

The equilibrium distribution functions and equilibrium forcing term can be written as a polynomial expansions to satisfy all constraints (15)–(18),

$$f_i^{eq}=A_s+B_s u_\alpha e_{i\alpha}+C_s u^2+D_s u_\alpha u_\beta e_{i\alpha}e_{i\beta}+G_{s\alpha\beta}e_{i\alpha}e_{i\beta},$$

$$g_i^{eq}=L_s+K_s u_\alpha e_{i\alpha}+J_s u^2+Q_s u_\alpha u_\beta e_{i\alpha}e_{i\beta},$$

$$h_i=T_s H_\alpha e_{i\alpha}, \quad (20)$$

where $s=\vec{e}_i^{\,2}\in\{0,1,2\}$ for the different absolute values of the velocities and the coefficients are

$$A_2=(p_0-k\phi\boldsymbol{\nabla}^2\phi)/8, \quad A_1=2A_2, \quad A_0=\rho-12A_2,$$

$$B_2=\rho/12,\quad B_1=4B_2,\quad B_0=0,$$

$$C_2=-\rho/16,\quad C_1=-\rho/8,\quad C_0=-3\rho/4,$$

$$D_2=\rho/8,\quad D_1=\rho/2,\quad D_0=0,$$

$$G_{2xx}=\frac{k}{16}[(\partial_x\phi)^2-(\partial_y\phi)^2],$$

$$G_{2xy}=G_{2yx}=\frac{k}{8}(\partial_x\phi\partial_y\phi),\quad G_{2yy}=-G_{2xx},$$

$$G_{1xx}=4G_{2xx},\quad G_{1yy}=4G_{2yy},\quad G_{1xy}=G_{1yx}=4G_{2xy},$$

$$L_2=\Gamma\mu/8,\quad L_1=2L_2,\quad L_0=\phi-12L_2,$$

$$J_2=-\phi/16,\quad -\phi/8,\quad J_0=-3\phi/4,$$

$$Q_2=\phi/8,\quad Q_1=\phi/2,\quad Q_0=0,$$

$$T_2=1/12,\quad T_1=4T_2,\quad T_0=0.$$

IV. RESULTS AND DISCUSSION

The simulations described above were carried out in two dimensions on a lattice that is 32×612 sites in size. The initial conditions for the order parameter distribution were chosen so as to provide a two-stream flow where the *A* fluid flows through the ''top'' part of the channel ($y>h/2$) and the *B* fluid flows through the ''bottom'' part of the channel ($y<h/2$). In the absence of the patterned substrate, the velocity profile is defined by the external pressure gradient $-f_p$; we obtained the steady flow profile that exactly coincides with the analytical solution $u_x=(1/2\eta)f_p y(h-y)$ and $u_y=0$. In all the simulations described below, we ''switch on'' the interaction inside boxes (1) and (2) when a steady-state Poiseuille flow is achieved. Periodic boundary conditions are imposed at the two ends of the channel; however, by having such a long channel after the patterned region, the order parameter distribution and velocity profiles are very similar at both the beginning and end of the channel and no additional perturbations are introduced as the fluid flows into the boxes [27].

If we equate the simulation parameters to typical experimental values, we can obtain a feel for the time and length scales that are modeled by our system. In particular, we make the following identifications: $\rho=10^3$ kg m^{-3}, $\eta=3\times10^{-3}$ kg m^{-1} s^{-1}, and pressure $p_0=10^5$ N m^{-2}. This then gives a time step of $\Delta t=\eta/p_0\approx3\times10^{-7}$ s, a lattice spacing of $\Delta x=t(p_0/\rho)^{1/2}\approx3\times10^{-6}$ m and channel width $h\approx10^{-4}$ m. The fluid velocity in the channel is $u_0\approx0.3$ m s^{-1} and the Reynolds number is $\mathrm{Re}=u_0h(\rho/\eta)\approx10$. Thus, we are in the range of interest for microfluidics.

In the presence of the patterned substrate and absence of the imposed flow ($f_p=0$), the equilibrium order parameter distribution inside each box mimics the design in the substrate. The characteristic time that is needed to reach the steady state can be roughly estimated as $t_0\approx h^2/(8CD)$ from a dimensional analysis of the convection-diffusion equation, assuming that the main term in the chemical potential for this process is the coupling term $\mu\approx2C(\phi-\phi_0)$. Here, we take the width of the patch $h/2$ to estimate the characteristic size.

In the presence of the imposed flow, each component is pushed into energetically unfavorable (or nonwettable) domains. The system tries to minimize its free energy by having the *A* stream flow across the channel to the *A* patch and the *B* stream traverse the channel to the *B* patch (see Fig. 1). As a consequence of this energy-minimizing motion, the two components are driven to flow into each other and thereby undergo mixing. It is this effective coupling of thermodynamics and dynamics that locally alters the phase behavior of the fluid. Examples of this behavior are shown in Fig. 2.

The mixing of the fluids occurs in broad regions between the patches, as can be seen in Figs. 2(a) and 2(b), where the white zones correspond to the *A* phase, the dark gray places mark the *B* phase, and the light gray areas correspond to the mixed phase. The actual values of the order parameter are shown in plots (c) and (d). The black arrows in Figs. 2(a) and 2(b) mark the direction and magnitude of the fluid velocity; the size of the arrows is proportional to the absolute value of the velocity.

The images in Figs. 2(a) and 2(b) reveal how flow couples to thermodynamics to produce the mixed phase. At the left edge of box 1, preferential wetting interactions drive each component to cross the channel and thereby mix in the center of the box. At the right hand side of box 1, the interactions have switched the positions of the *A* and *B* stream. At this point, the interactions imposed by box 2 have a critical effect. As the fluids approach this neighboring box, the liquids are once more confronted with energetically unfavorable domains. Consequently, some of the fluid flows away from the boundary and back into box 1, thus promoting mixing. The latter behavior contributes to large areas of light gray between boxes 1 and 2 (see Fig. 2). The flow in the *x* direction transports the fluid from box 1 to box 2, including the liquid that was mixed in box 1. At the same time, arrows at the top and bottom at the left edge of box 2 indicate that each component is again driven across the channel to reach the respective wettable domains. The motion provides another opportunity for mixing the fluids and contributes to enhancing the size of the $\phi\approx0$ region in box 2.

In addition to visualizing the state of the system from the above figures, we can quantify the degree of mixing inside the channel by defining the ''region of mixing'' *R* at the each site along the channel. This parameter is given by

$$R(x)=\sum j, \tag{21}$$

where we sum the number of lattice sites *j* along the *y* direction in which the liquid is defines as ''mixed.'' We define the condition for being mixed as: $|\phi|<\phi_{mix}$, where ϕ_{mix} is the maximum order parameter value that we associate with the mixed state. In all the plots of *R* described below, we took $\phi_{mix}=0.2\phi_0$.

The region of mixing for three different velocities at steady state is shown in Fig. 3; curves 1 and 2 describe the cases shown in Figs. 2(a) and 2(b), respectively, while curve

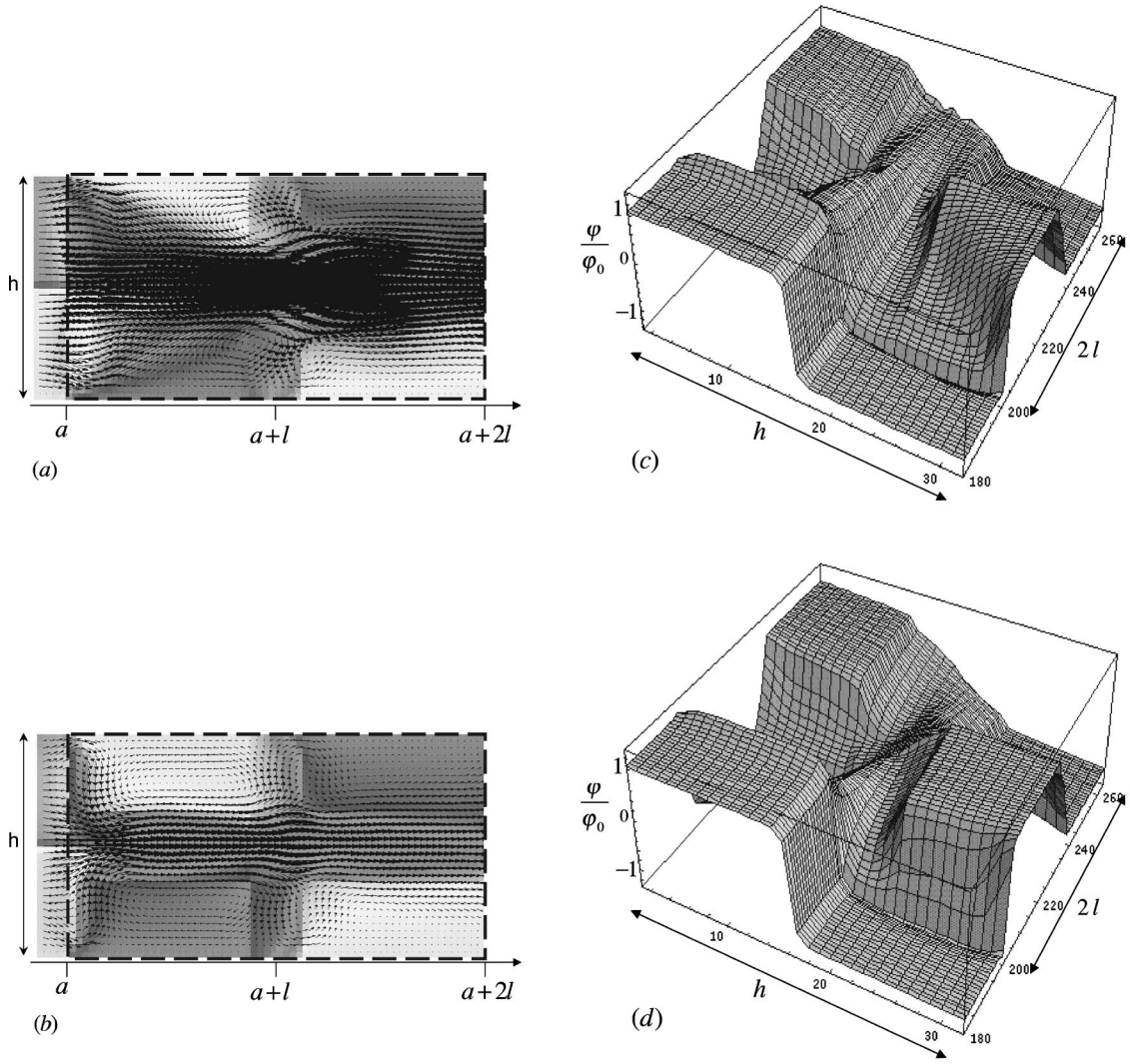

FIG. 2. Simulation results showing the distribution of the order parameter in the system at steady state; the length of each box is $l=32$ (here and in the following figure captions, all lengths are dimensionless and expressed in units of lattice sites). Fluid parameters are $\lambda=1.1$, $k=0.01$, $T=0.5$, $D=0.3$, $\eta=0.1$. Parameters for the interaction potential are $C=0.04$; $r=7$; $\delta_1=4$; $\delta_2=5$. The external pressure gradient is $f_p=4\times10^{-5}$ [in (a) and (c) and $f_p=2\times10^{-5}$ in (b) and (d)]. The different shading corresponds to the different values of order parameter in (a) and (b) (the *A* phase is dark gray, the *B* phase is white). The absolute values of the order parameter is further displayed in (c) and (d). In (a) and (b) arrows mark the direction and magnitude of the velocity field: the size of the arrow is proportional to the magnitude of the velocity.

3 corresponds to the case with the lowest velocity ($f_p=10^{-5}$). The best mixing occurs in the second box for the highest of the three velocities (curve 1). As compared to curve 1, decreasing the imposed pressure gradient (and thus the velocity) by a factor of 2 (curve 2) results in better mixing in the first box and lower mixing in the second box. We note that in curve 2, the degree of mixing between boxes 1 and 2 is relatively the same. If we keep decreasing the velocity, thermodynamics begins to win and the order parameter distribution is mainly defined by the static interaction of the fluid with patches. The dynamics do however lead to a short area of mixing at the beginning of each box (curve 3). It is important to note that increasing the velocity beyond the value for case 1 ($f_p=4\times10^{-5}$) also leads to poor mixing. For very high velocities, the fluid hardly ''feels'' the substrate, resulting in only small distortions of the order parameter distribution.

To obtain insight into the dynamic behavior of the systems in Fig. 3, we calculate the average value of the order parameter as a function of time inside each box. The average order parameter M_i is given by

$$M_i=\frac{\sum |\phi/\phi_0|}{lh}, \tag{22}$$

where the index i takes on the value of 1 or 2, indicating the appropriate box, and the summation is made over the all lattice sites inside that box. Here, h is the width of the box and l is the length. Figure 4 shows such plots for the cases

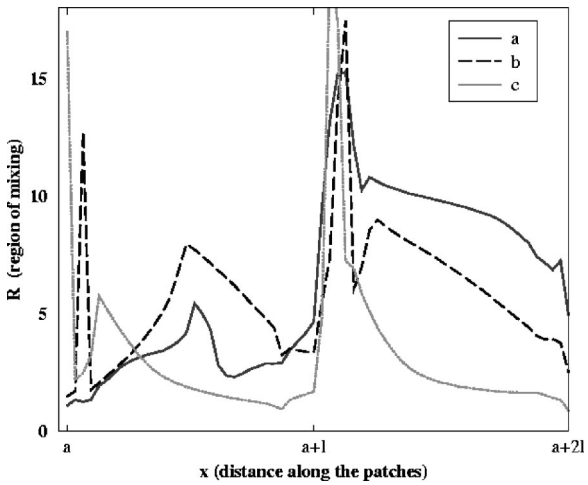

FIG. 3. Region of mixing along the boxes for the different velocities at the steady state: (a) $f_p=4\times10^{-5}$; (b) $f_p=2\times10^{-5}$; (c) $f_p=10^{-5}$. All other parameters are the same as in Fig. 2

corresponding to curves 1 and 2 in Fig. 3; the solid lines mark the behavior in box 1 and the dashed lines indicate the behavior in box 2. There are a number of interesting observations that emerge from the plots. In particular, the average order parameter in the first box, M_1, has a minimum at early times; this time is the same for all the values of the imposed pressure gradient (i.e., velocities). This minimum is deeper for the lower velocity. The steady-state value of M_1 is slightly lower for the higher velocity. The values of the average order parameter in the second box M_2 decrease smoothly with the time.

For both cases described above, the steady-state value of the average order parameter is lower in the second box than in the first box ($M_2<M_1$), indicating a greater degree of mixing in the second box. This observation is consistent with the larger regions of mixing seen in box 2 (Fig. 3). As we noted above, in box 2 not only do the fluids cross the channel to reach the respective wettable domains but also, the flow in

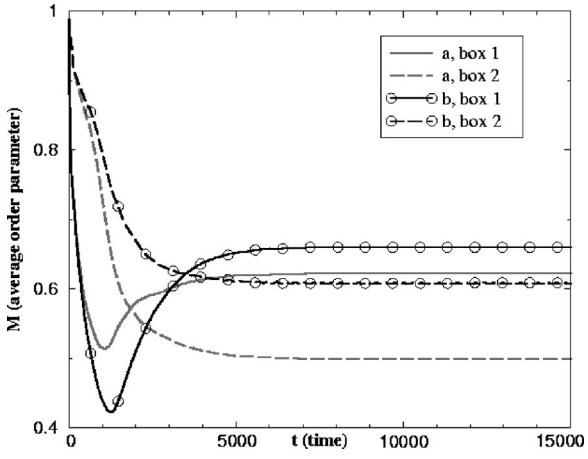

FIG. 4. Average order parameter vs time in the first box M_1 (solid curves) and in the second box M_2 (dashed curves) for the different velocities at the steady state: (a) $f_p=4\times10^{-5}$; (b) $f_p=2\times10^{-5}$. All other parameters are the same as in Fig. 2.

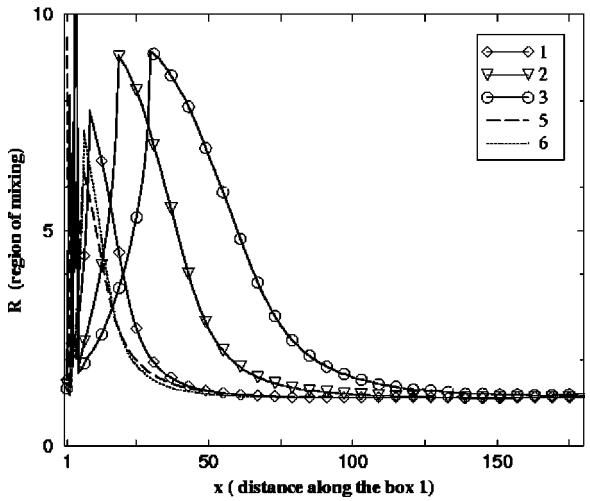

FIG. 5. Region of mixing in the first box for the long boxes $l=200$; (1) $D=0.6$, $\eta=0.1$, $f_p=2\times10^{-5}$; (2) $D=0.3$, $\eta=0.1$, $f_p=2\times10^{-5}$; (3) $D=0.15$, $f_p=2\times10^{-5}$; (4) $D=0.3$, $\eta=0.1$, $f_p=10^{-5}$; (5) $D=0.3$, $\eta=0.2$, $f_p=2\times10^{-5}$. All other parameters are the same as in Fig. 2.

the x direction transports already mixed fluid from box 1 into the second box. The latter phenomenon contributes to the higher state of mixing in box 2.

The above observations highlight the utility of the checkerboard pattern in promoting the mixing of the fluids. Forcing the fluids to intersect across one set of boundaries (as in box 1) can promote mixing, but the overall degree of mixing is improved if the fluids are confronted by an additional set of boundaries, which once again drive the fluids to flow into each other. Another important architectural feature that will influence the fluid properties is the length of each box. In the above simulations, the length of each box was equal to the width of channel. We expect that thermodynamic effects will dominate at the ends of long boxes. We now define a correlation length l_{corr} as the length over which the thermodynamic distribution is distorted by the imposed flow field. In terms of the simulation, we estimate this length from the plots of R versus X. For example in Fig. 4, we take l_{corr} as the length beyond the large peak and at the point where R first reaches the apparent small saturated value. From a simple dimensional analysis, one can argue that this length should be proportional to the fluid velocity u_0 multiplied by some characteristic time t_0. It is reasonable to assume that t_0 is inversely proportional to the diffusivity D even in the presence of an imposed flow [28]. Thus, we hypothesize that l_{corr} scales approximately with u_0/D. For the characteristic velocity u_0, we can take the velocity in the middle of the channel caused by the imposed flow $u_0=(1/8\eta)f_p h^2$ before the boxes. As we show below, the simulations support this observation.

To determine the values of l_{corr} for our system, we perform simulations using very long boxes. In particular, we take $l=200$. In this way, we ensure that l is greater than l_{corr} and the end of each box displays the order parameter distribution that corresponds to the thermodynamic solution. Figure 5 shows the region of mixing at steady state inside the

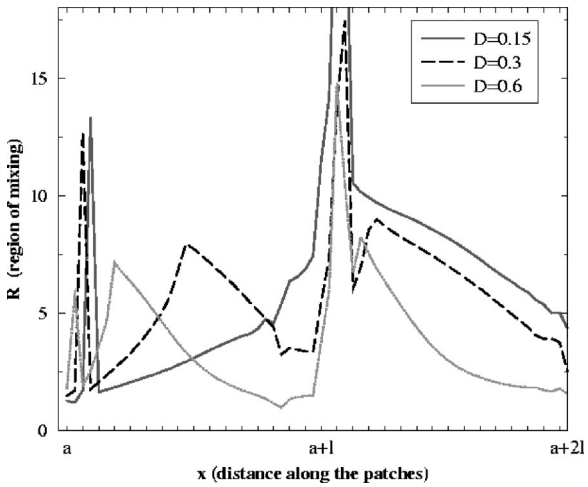

FIG. 6. Region of mixing along the boxes for the different diffusion coefficients as marked in the figure. All other parameters are the same as in Fig. 2

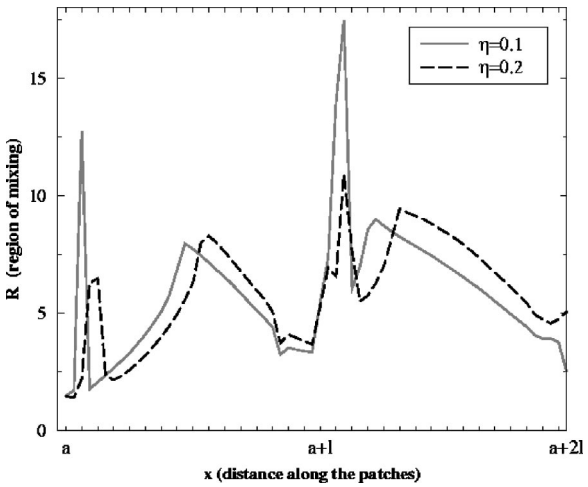

FIG. 7. Region of mixing along the boxes for the different viscosities: (1) $f_p=2\times10^{-5}$; $\eta=0.1$ (2) $f_p=4\times10^{-5}$; $\eta=0.2$. All other parameters are the same as in Fig. 2.

first long box ($l=200$) for various fluid diffusivities and imposed velocities.

Increasing the diffusivity D by a factor of 2 (curve 1, Fig. 5) relative to reference case (curve 2) leads to an approximate two-fold decrease in l_{corr}, as well as a decrease in the maximum value of R. Comparable decreases in l_{corr} and changes in the order parameter distribution can be obtained by decreasing the velocity in the middle of the channel, either by halving the external pressure gradient (curve 5) or doubling the fluid viscosity (curve 6). On the other hand, decreasing the diffusivity D by a factor of 2 leads roughly to a doubling of l_{corr} (curve 3).

Knowledge of the correlation length l_{corr} for a particular system tells us the length beyond which there is essentially no mixing within a box. The information also provides insight into the optimal placement of the second (or subsequent) boxes. In particular, choosing the length of box 1 equal to l_{corr} is not the best choice for optimal mixing because the region of mixing is maximal in the middle of that length and decays at the end of l_{corr}. One of the best cases for optimal mixing in both boxes is to take the length of each box $l\approx l_{corr}/2$. This is the situation captured in Fig. 2(b). The length of each box in Fig. 2(a) is $l\approx l_{corr}/4$ since the imposed pressure gradient is two times higher than in Fig. 2(a). Thus, based on an estimation of l_{corr}, it is possible to choose such box lengths that will provide effective mixing for the specific fluids and for the chosen range of velocities.

Having determined the optimal geometry for the underlying substrate, we now investigate how the fluid characteristics affect the degree of mixing on a fixed surface pattern. In particular, we again take the length of each box to be equal to the width of the channel and determine how variations in the diffusivity D and viscosity η affect the region of mixing in the system. Figure 6 shows plots of R along the patches for three values of D at a fixed velocity. The plots reveal that the fluid with the smallest value of D provides the broadest region of extensive mixing. Recall that D is a coefficient in the convection-diffusion equation and a large value of D implies that the system is dominated by thermodynamics. In other words, the order parameter distribution is closer to the thermodynamic solution, except at the regions near the beginning of each box. Conversely, for small values of D, the system is more sensitive to the effects of the imposed flow field.

We use Fig. 7 to demonstrate an important aspect of varying the viscosity of the solution. In particular, similar degrees of mixing can be attained for fluids with different viscosities by appropriately modifying the imposed pressure gradient. Specifically, we consider the cases of $\eta=0.1$ and 0.2. If we apply a two-fold greater pressure gradient to the $\eta=0.2$ case, we obtain the same velocity profile before the boxes as in the $\eta=0.1$ case. Consequently, the order parameter distribution and the region of mixing is similar for both situations. Thus, increases in the imposed pressure can be used to tailor the degree of mixing for high viscosity fluids.

V. CONCLUSIONS

Through the above simulations, we examined the effect of an imposed flow field on a binary mixture that lies above a patterned substrate and is confined in a microchannel. The results reveal that the coupling of hydrodynamics and thermodynamics can be exploited to control the phase behavior of the fluids. Specifically, the immiscible components can be driven to form a homogeneous mixture in a broad region of the confining channel. We showed that a checkerboard pattern of wettable and nonwettable domains was an effective surface design for promoting the mixing. By examining the flow patterns and order parameter distribution in a given ''box,'' we determined the optimal box length for maximizing the degree of mixing within the system. In particular, a box length of $l\approx l_{corr}/2$ proved to be highly effective. We showed that l_{corr}, the length scale over which the thermodynamic distribution is distorted by the imposed flow field, is dependent on the imposed velocity and the diffusivity of the material. Based on an estimation of l_{corr}, it is possible to fix a box length that will optimize the performance of the ''mix-

ing station'' for the specific fluids and range of velocities under consideration.

For a fixed box length, we examined the effect of modifying the diffusivity and viscosity of the fluid. The findings indicate how the materials properties affect the extent of mixing and how the imposed flow field can be altered to manipulate the behavior of the fluid.

The above calculations were performed in two dimensions. Typically, the widths of the microchannels in microfluidic devices are five to ten times greater than the height of the systems. In the latter case, the system can be considered as roughly two dimensional. In three dimensions (3D), the interplay between wetting and hydrodynamic boundary conditions can potentially lead to interesting additional physics. Work is currently in progress to investigate the behavior of the system in 3D. Meanwhile our findings indicate that patterned substrates can provide an effective, nonmechanical means of mixing solutions and open the possibility of creating spatially localized reaction chambers within microfluidic devices.

[1] J. Knight, New Sci. **159**, 28 (1998).
[2] S. Dietrich, J. Phys.: Condens. Matter **8**, 9127 (1996); Phys. **l57**, N3 (1996).
[3] C. Bauer and S. Dietrich, Phys. Rev. E **60**, 6919 (1999).
[4] S. Puri and S.L. Frisch, J. Phys.: Condens. Matter **9**, 2109 (1997).
[5] S. Bastea, S. Puri, and J.L. Lebowitz, Phys. Rev. E **63**, 041513 (2001).
[6] M.K. Chaudhury and G.M. Whitesides, Science **256**, 1539 (1992).
[7] A. Karim *et al.*, Phys. Rev. E **57**, R6273 (1998); **16**, 3474 (2000).
[8] J.S. Rowlinson, and B. Widom, *Molecular Theory of Capillarity* (Clarendon Press, Oxford, 1982).
[9] D. Kataouka and S. Troian, Nature (London) **402**, 794 (1999).
[10] A. Papra *et al.*, Langmuir **17**, 4090 (2001).
[11] C. Bain, G.D. Burnetthall, and R.R. Montgomerie, Nature (London) **372**, 414 (1994).
[12] S.W. Lee and P.E. Laibinis, J. Am. Chem. Soc. **122**, 5395 (2000).
[13] H. Gau, S. Herminghaus, P. Lenz, and R. Lipowsky, Science **283**, 46 (1999).
[14] B.S. Gallardo *et al.*, Science **283**, 57 (1999).
[15] C. Rascon and A.O. Parry, Nature (London) **407**, 986 (2000).
[16] S. Chen and G.D. Doolen, Annu. Rev. Fluid Mech. **30**, 329 (1998).
[17] N.S. Martys and H. Chen, Phys. Rev. E **53**, 743 (1996).
[18] We note that for the pharmaceutical and cosmetics industries, microfluidic assays commonly require the formation of stable emulsions of immiscible fluids, such as oil and water.
[19] J.L. Wilbur *et al.*, Nanotechnology **7**, 452 (1996).
[20] B. Zhao, J. Moore, and D.J. Beebe, Science **291**, 1023 (2001).
[21] L.D. Landau and E.M. Lifshitz, *Fluid Mechanics*, 2nd ed. (Pergamon Press, Oxford, 1987).
[22] M.R. Swift, E. Orlandini, W.R. Osborn, and J.M. Yeomans, Phys. Rev. E **54**, 5041 (1996).
[23] A.C. Balazs *et al.*, J. Phys. Chem. B **104**, 3411 (2000).
[24] O. Kuksenok, J. M. Yeomans, and A. Balazs, Langmuir **17**, 7186 (2001).
[25] A. Onuki, J. Phys.: Condens. Matter **9**, 6119 (1997).
[26] C. Denniston, E. Orlandini, and J.M. Yeomans, Europhys. Lett. **52**, 481 (2000).
[27] When the fluids interact with the boxes, there is a decrease in the fluid velocity. Thus to maintain a constant Poiseuille profile for the velocity distribution before the boxes, we correct the values of the velocity at the beginning of the box according to the analytical solution cited above.
[28] We found that in all simulations, the characteristic time that is needed to rich the steady-state can still be roughly estimated as characteristic time t_0 for the static case. This is most likely due to the fact that we are in the limit of relatively high values for D.